



**A study of buried channel formation in oxidized porous silicon**

Journal:	<i>RSC Advances</i>
Manuscript ID:	RA-ART-09-2014-010547.R1
Article Type:	Paper
Date Submitted by the Author:	23-Oct-2014
Complete List of Authors:	Dang, Zhiya; National University of Singapore, Physics Liu, Dongqing; National University of Singapore, Physics Azimi, Sara; National University of Singapore, Physics Breese, Mark; National University of Singapore, Physics

**A study of buried channel formation in oxidized porous silicon**

Z. Y. Dang, D. Q. Liu, S. Azimi, M. B. H. Breese\*

*Centre for Ion Beam Applications (CIBA), Department of Physics, National University of Singapore**Singapore 117542***Abstract**

We have studied the formation of buried, hollow channels in oxidized porous silicon produced by a process based on focused high-energy ion irradiation of low resistivity, p-type silicon. This is followed by electrochemical anodization and various oxidation stages, all of which may influence the channel size, shape and roughness. We have identified several mechanisms by which the irradiation fluence can alter the channel size and shape, and studied the dependence on anodization current density and oxidation temperature. A low anodization current density combined with high temperature oxidation results in hollow channels in oxidized porous silicon being shrunk to dimensions of about 50 nm. Highly smooth, symmetric channels are produced using viscous flow of the oxidized porous silicon during high temperature oxidation.

\* Contact author: Mark Breese

Email: [phymbhb@nus.edu.sg](mailto:phymbhb@nus.edu.sg)

## 1. INTRODUCTION

We recently developed a process<sup>1</sup> for producing buried micro- and nano-scale hollow channels in fully oxidized porous silicon (FOPS). This process is based on focused, high energy ion irradiation in a nuclear microprobe<sup>2</sup> of low resistivity, 0.02  $\Omega$ .cm, p-type silicon, where the defect generation rate peaks close to the ion end-of-range depth, see figure 1a. Focused ion beam irradiation, typically with protons or helium ions, results in a small volume at the end-of-range depth being highly damaged, while the portion closer to the surface is damaged to a lesser extent. High energy ion irradiation therefore allows volumes which are localized in both position and depth to be selectively damaged, figure 1b. Such damage is mostly in the form of vacancy-interstitial pairs (Frenkel defects), some of which reduce the density of free charge carriers within the doped silicon. Consequently for high fluence ion irradiation the end-of-range regions are fully depleted of charge carriers and do not undergo anodization, resulting in the formation of silicon regions surrounded by porous silicon<sup>3-5</sup>. For low fluence ion irradiation these end-of-range regions are only partially depleted of charge carriers and during subsequent electrochemical anodization in hydrofluoric acid (HF) solution (24% HF, from a 1:1 solution of HF (48%):ethanol), they become much more porous than the surrounding unirradiated porous silicon (PS) by a process of increased current flow and increased resistivity<sup>1,6,7</sup>, figure 1c,d. After rinsing in ethanol and then in distilled water for 5 minutes, the sample undergoes room temperature (RT) oxidation for about two weeks, after which the highly porous end-of-range regions may be selectively removed in dilute HF as they become fully oxidized, while the surrounding matrix is barely affected owing to its lower porosity, figure 1e. Such PS structures containing buried hollow channels may now be turned into a similar structure in partially or fully oxidized porous silicon by high temperature (HT) oxidation, figure 1f.

Micro- and nanofluidics<sup>8</sup> rely on the ability to fabricate grooves and hollow channels as the basic building blocks of structures and devices<sup>9, 10</sup>. Polymers such as PDMS are widely used but have limitations when the channel diameter is reduced as they suffer from swelling which reduces the channel area or even completely closes it. Micromachined channels in electrically insulating and optically transparent materials such as glass and quartz have become more important<sup>11</sup> in areas such as DNA analysis<sup>12</sup>. Furthermore, glass and quartz carry a negative surface charge, which has the advantage of net negatively charged biomacromolecules such as DNA being not electrostatically adsorbed.

Oxidized porous silicon (OPS) is a form of glass and has many ideal properties for experiments involving fluid flow through micro and nano-scale channels, e.g. it is transparent and does not swell. In<sup>1</sup> we produced nanoslit channels of approximate dimensions 100 nm height  $\times$  1000 nm width in PS, after RT oxidation the sample was oxidized at 1000  $^{\circ}$ C to produce FOPS. These buried channels were

integrated with large reservoirs for DNA linearization studies. While this proved the concept and validated the process, there were several aspects which were poorly understood and not optimized which we seek to address here. One aspect is how small and how reliably can we make the hollow channels of widths of 100 nm or less ? To answer this a much better understanding of the behaviour of both the unirradiated host PS and the irradiated volume at the end-of--range is required.

In <sup>1</sup> we described how this process could be used to form buried hollow channels running parallel to the surface and also connecting vertical channels perpendicular to the surface, using different regimes of ion energy and fluence. Here we confine our study to buried, end-of-range channels but the conclusions reached equally apply to producing vertical channels. We divide this paper into studies of different parts of this process, namely:

- In unirradiated silicon wafers we study effects of different anodization current density  $j$  and HT oxidation temperature  $T$  on the PS porosity, OPS layer thickness and surface roughness.
- We study the selective removal of high porosity PS from the end-of-range region after RT oxidation to find how the resulting hollow channel shape and size depends on the number of removal steps, RT oxidation time and HF concentration.
- We study the effect of fluence on channel formation. In particular how any residual crystalline or low porosity core beneath the hollow channel produced by different fluences affects the channel shape after HT oxidation. We also consider how the zone of increased resistivity along the initial portion of the ion trajectory affects channel formation for different fluences.
- We study channel formation in partially or fully oxidized PS after HT oxidation for different  $T$ ,  $j$  and fluence. We aim to find whether different regimes of  $j$  result in channel shapes and sizes which are unaffected by HT oxidation at a lower  $T$  or which can be controllably reduced in size to produce smaller, nanoscale channels at a higher  $T$ . and whether the hollow channels can form smooth, circular or elliptical cross-sections during HT oxidation at high  $T$ .

## 2. REVIEW OF OXIDIZED POROUS SILICON (OPS)

There exists a significant body of work on the oxidation of porous silicon as it was important in the development of Full Isolation by Porous Oxidized Silicon (FIPOS) technology and other work requiring a dielectric isolation on silicon <sup>13</sup>. The quality and properties of OPS depends on many factors during the electrochemical anodization and HT oxidation steps <sup>14-16</sup>. For microelectronics applications where optimal

dielectric quality, mechanical and chemical reliability of the OPS layer is required then the conditions need to be highly optimized towards these goals. However, for our process we do not have the same requirements on the OPS layer quality, which only needs to be suitably transparent for optical inspection and low enough in roughness and porosity to allow unhindered fluid flow and no loss through micro- or nano-scale channel dimensions.

In our process there is also an intermediate RT oxidation step, see figure 1e. In Ref. <sup>17</sup> studies of RT oxidation of PS show that it proceeds slowly in a dry atmosphere but much faster in wet air. Oxidation in liquids such as methanol and ethanol occurs a hundred times faster than in water <sup>18</sup>. A solution containing an oxidizing agent such as noble metal ions exhibits the highest oxidizing ability. Oxygen is a mild oxidant under RT conditions.

Since SiO<sub>2</sub> has longer bond lengths compared to silicon, OPS tends to increase in volume during HT oxidation. PS with a low porosity layers tend to expand whereas higher porosity layers tend to contract, a porosity  $P = 56\%$  results in minimum volume change <sup>14</sup>. A two-step process is normally utilized for HT oxidation <sup>15</sup>, usually performed in a standard oxidation furnace under atmospheric pressure in dry oxygen <sup>14,15</sup>, or in pyrogenic steam under atmospheric pressure. First, a pre-oxidation step at low temperature, around 300 °C, for one hour is used to stabilize the texture against restructuring during subsequent heat treatment. Second, a HT oxidation step where one or more temperatures may be used to ensure complete oxidation of the PS layer with minimal residual stress. HT oxidation involves two processes, oxidation of silicon within the porous layer and densification of the resulting silica. The two steps may occur simultaneously at high temperatures. The first process depends only on the porosity  $P$  and the oxidation temperature  $T$ . PS of porosity  $P \sim 56\%$  is required to ensure a good quality OPS with minimal residual Si crystallites <sup>15</sup>. For  $T \leq 1000$  °C, the resultant OPS retains a certain porous character. For  $T \geq 1000$  °C, oxide densification occurs and viscous flow of silica can occur. In Ref. <sup>14</sup> it was concluded that densification rather than oxidation was the critical step in producing high quality oxides.

Oxidation occurs throughout the whole volume of the porous layers, and the same kinetics are obtained for layers of different thicknesses, at least up to 10 μm. Complete oxidation is achieved only if the PS has an initial  $P > 46\%$ . Within the temperature range of 700 to 850 °C the thickness of the OPS is always greater than the PS layer <sup>14</sup> even for an initial  $P > 56\%$ , indicating that within this temperature range the OPS remains porous after oxidation.

Apart from reducing the amount of silicon, HT oxidation induces stress and strain in the grown SiO<sub>2</sub> and the residual silicon <sup>16</sup>. Besides the thermal stress, a large intrinsic stress accumulates at the Si–SiO<sub>2</sub> interface because of the different Si–Si and Si–O bond lengths. TEM analysis has verified the

presence of amorphous SiO<sub>2</sub> in the porous structure; the growth of crystalline SiO<sub>2</sub> requires either higher temperatures, above 1200 °C, long reaction times (hundreds of hours), high pressures or a catalyst. Lattice deformation is induced by a thermal expansion coefficient mismatch between the grown SiO<sub>2</sub> and the residual Si, changes in the relative lattice deformations increase with  $T$ . The formed oxide inhibits the relaxation of the remaining PS skeleton; only when the amount of residual silicon is low enough (~20%) can the structure relax. Additionally, the relief of stress by viscous flow of SiO<sub>2</sub> at  $T > 950$  °C could reduce its effect on oxidation inhibition kinetics, according to Ref. <sup>19</sup>, thus, speeding up the oxidation rate.

### 3. CHARACTERIZATION OF UNIRRADIATED WAFERS

An important aspect of this process is the choice of wafer resistivity, which determines whether irradiation and anodization can induce a sufficiently increased porosity at irradiated regions. This aspect was discussed in Ref. <sup>1</sup>. Figure 2(a) shows the porosity of different resistivity p-type silicon after anodization, data taken from Ref <sup>6</sup>. A wafer resistivity of about 0.02 Ω.cm is ideal in providing a wide range of porosity versus  $j$  and also for other reasons we previously discussed <sup>1</sup>. The range of  $j$  we consider in this paper is from 30 to 300 mA/cm<sup>2</sup>, indicated by the double headed arrow.

#### 3.1. OPS THICKNESS FOR DIFFERENT $j$ & $T$

Characterization of the OPS layer thickness change versus  $j$  during HT oxidation is central to our fabrication process, so before considering how ion irradiation alters the anodization and various oxidation processes we first study the effects of  $j$  and  $T$  on the OPS layer thickness and quality for unirradiated wafers. We confine ourselves to a HT oxidation temperature range of  $T = 800$  to 1000 °C. Below 800 °C the silicon oxidation rate is too low, around 20 nm after 11 hours at 700 °C in dry oxygen, compared with 85 nm after 30 minutes at 1100 °C <sup>20</sup>. As described in section 2, at  $T = 800$  °C the OPS may not be completely oxidized at low  $P$ , remaining porous and containing many silicon crystallites. Under these conditions, since the OPS should not undergo viscous flow at this temperature <sup>16</sup>, the resultant channel shape and size is expected to remain unchanged after oxidation.

At  $T = 1000$  °C the OPS layer is expected to be completely oxidized <sup>15</sup>, and to undergo viscous flow <sup>21</sup>. We do not study higher temperatures as we expect the OPS layer to become too fluid, destroying any hollow channels. We confine ourselves to a HT oxidation period of two hours, long enough to reach a final oxidation state of the PS layer under most conditions <sup>14</sup>. This time is long enough to fully oxidize any remaining small silicon cores of dimensions of hundreds of nanometres but not larger, micrometer size cores.

Figure 2b plots the measured change in thickness of a PS layer versus  $j$  before and after HT oxidation at 1000 °C for 2 hours. As expected, for low  $j$  the OPS layer thickness increases after oxidation while at high  $j$  it reduces. This data was used to construct a plot of porosity  $P$  of the anodized layer versus  $j$ , figure 2c. We assume the PS has been completely oxidized at high temperature and that the OPS is completely densified. These assumptions may not be fully correct for low  $j$ , as described above, but the figure still serves as a guide to the change of OPS thickness expected under our processing conditions.

Under these conditions a value of  $j \sim 70\text{mA/cm}^2$  gives an unchanged layer thickness, where  $P = 56\%$ . However, for our process the value of  $j$  which results in zero change in layer thickness after HT oxidation will be slightly lower than this since the RT oxidation stage slightly increases the porosity of the host PS. For example, we measured an increase in porosity of a PS layer anodized at  $j = 60\text{mA/cm}^2$  from  $P = 53\%$  to  $59\%$  after 2 weeks RT oxidation. Values of  $j$  down to  $40\text{ mA/cm}^2$  ( $P \sim 50\%$ ) are used where the OPS expands at low  $T$ . High values of  $j = 150\text{ mA/cm}^2$  ( $P \sim 68\%$ ) and even  $j = 300\text{ mA/cm}^2$  ( $P \sim 75\%$ ) are used where the OPS contracts at high  $T$ . Even at the lowest  $j$  used here, complete oxidation is expected for HT oxidation at  $T = 1000\text{ °C}$  since the PS has an initial porosity higher than  $P \sim 46\%$ , as discussed in section 2.

Figure 2d shows the PS layer thickness versus  $T$  during HT oxidation after anodization with fixed values of  $j$ . For  $j = 40\text{ mA/cm}^2$  the OPS layer becomes thicker at low  $T$  (800 , 900 °C), before reducing at higher  $T = 1000\text{ °C}$ , though still thicker than its original value. The behaviour differs from that for higher  $j$ ; for  $j = 150\text{ mA/cm}^2$  the OPS layer thickness is unchanged up to 900 °C, whereas for  $j = 300\text{ mA/cm}^2$  there is a noticeable compaction even at 900 °C.

This plot demonstrates the different regimes which can be achieved by varying the anodization and oxidation conditions, both of which influence the size and shape of the buried channels in OPS. Even at low  $j$  the OPS layer is likely to be fully oxidized during HT oxidation at  $T = 1000\text{ °C}$ , so it should undergo viscous flow; we aim to study whether this leads to increased channel dimensions when the OPS layer expands. At high  $j$  the OPS layer is even more likely to be fully oxidized and so to undergo viscous flow and compaction at a lower temperature during HT oxidation, for  $T \geq 900\text{ °C}$ . We study whether this provides a mechanism to reduce the channel dimensions. For a low  $T < 900\text{ °C}$  where the OPS layer may not be fully oxidized, the channel dimensions are likely to remain unchanged whatever the value of  $j$ , and we aim to study whether this provides a stable, predictable regime for channel formation.

### 3.2. ROUGHNESS & POROSITY OF OPS

While we do not consider effects of ion irradiation on channel formation in this section, to illustrate the important point regarding the lower density and quality of OPS which may be produced compared to that of a thermally grown oxide, Figure 3a shows a SEM image of a cores in PS formed at the end-of-range region of 250 keV proton irradiation with a high line fluence of  $10^{11}$  ions/cm, and anodized at  $j = 50$  mA/cm<sup>2</sup>. A solid silicon core appears as a bright area against the darker, grainy background of the PS host. Fig. 3b shows the same cores after HT oxidation at 1000°C for 3 hours. The silicon core size reduces after HT oxidation, with its outer volume converted into SiO<sub>2</sub> (appears bright) and the surrounding PS host converted to FOPS. While the SiO<sub>2</sub> layer appears smooth and free of voids and cracks, clearly the surrounding FOPS retains a porous character, as expected for HT oxidation temperatures of 1000 °C or lower.

Figure 4 considers another important effect of the formation of micro- and nano-scale channels by this process, which is the OPS surface roughness. Figure 4a shows a AFM (atomic force microscope) image at high  $j$  and HT oxidation at a low  $T = 750$  °C for 4 hours. The OPS comprises grains of typically 30 nm diameter at low  $j$ , which increase in size up to around 100 nm at high  $j$ . This is important limitation in considering whether one can form nanoscale channels with diameters less than the typical grain size of the OPS and for fluid flow through channels with rough surfaces. Figure 4b plots the r.m.s. (root mean square) OPS surface roughness versus  $j$  extracted from  $2 \times 2 \mu\text{m}^2$  areas of similar AFM images for a high  $T = 1000$  °C. At low  $j$  the surface roughness is only 0.4 nm r.m.s., and although the surface roughness still increases with  $j$  it clearly remains very smooth over the full range, increasing only to 1.7 nm at high  $j$ . We consider that the much smoother surface produced at high  $T$  is largely due to viscous flow of the OPS, and we conclude that  $T$  is a very important parameter in producing smooth channel surfaces in OPS. It should be as high as possible, commensurate with other process considerations, if channel roughness is critical.

### 4. EFFECTS OF ION IRRADIATION

We study hollow channel formation by writing long irradiated lines, then cleaving them for cross-section imaging after the various processing stages. See supporting information for definition and discussion of line fluence which is used through this paper. We use proton energies of either 100 keV (range of 850 nm in silicon) or 250 keV, (range of 2400 nm in silicon), see figure 1a. Higher fluences are generally required at higher proton energies as the lateral beam spread at the end-of-range increases, so the defect density decreases. The lateral beam spread is  $\sim 100$  nm and  $\sim 200$  nm FWHM (full-width-at-half-maximum) respectively for 100 and 250 keV protons in silicon. In several of the studies in this section a very high

current density of  $j = 300 \text{ mA/cm}^2$  is used. This is because some of the effects under discussion only become apparent at higher  $j$ , it is not to imply that this is the best  $j$  to use for channel formation.

#### 4.1. EFFECTS OF DIFFERENT ION FLUENCES

Unlike the example shown in Figure 3 where a high line fluence was used to fully deplete the end-of-range region and so form a solid silicon core after anodization, our process uses a low fluence to partially deplete the ion end-of-range region. Figure 5 shows the effect of varying the line fluence on formation of the hollow channel at low fluences or solid silicon core at higher fluences for irradiation with 100 keV protons from  $2 \times 10^9$  ions/cm to  $1 \times 10^{11}$  ions/cm, then anodized at  $j = 300 \text{ mA/cm}^2$ . The high porosity PS was removed after two weeks RT oxidation by brief immersion in 2% HF. At the lowest fluence of  $2 \times 10^9$ /cm a small hollow channel is formed with a residual silicon core at the base<sup>3,4</sup>. The core size increases with fluence, Figure 5b, as does the zone of highly porous silicon above it as shown from the larger hollow channel produced. For higher fluences, Figure 5c,d, a darker zone above the core region is arrowed, caused by a high defect density even along initial portion of the trajectory. Under these conditions this region also becoming highly porous and eventually collapsing at higher fluences, Figure 5e,f. This figure shows that important effects occur below (crystalline or low porosity core) and above (increased porosity) any hollow channel and both are studied in this section.

#### 4.2. RT OXIDATION STAGE

Figure 6 presents selected results of a study of selective removal of RT oxidized PS around the end-of-range where the RT oxidation time, frequency and duration in HF was varied. The aim is to find whether prolonged immersion in HF or additional RT oxidation stages result in more efficient removal of the highly porous silicon at the end-of-range. Samples were irradiated with different line fluences, then anodized at  $j = 300 \text{ mA/cm}^2$ . After two weeks RT oxidation the oxidized PS was removed with 24% HF for 30 minutes. The first batch of samples (left image) was immediately re-immersed in 24% HF for 14 hours, while a second batch (right image) underwent a second RT oxidation stage for one more week, then re-immersed in 24% HF for 4 hours. Clearly samples in the second batch have a larger hollow core, from which we conclude that an additional RT oxidation stage significantly enlarges the size of the resultant hollow core whereas additional time soaking in the HF solution produces little effect. We interpret this as the RT oxidation process saturating after a certain period where all exposed PS surfaces are covered with oxide. Oxide removal in the second batch exposes a fresh PS surface to further RT

oxidation. In comparison, in the first batch once oxide removal is completed then the HF solution does not remove any unoxidized Si.

#### 4.3. EFFECTS BELOW THE END-OF-RANGE REGION

We now present a study of the effects of different fluences on the core and channel shape and size formed after anodization, RT oxidation and HT oxidation. Figure 7, left-hand column, shows the channels in PS after irradiation with different fluences of 250 keV protons and anodization at  $j = 150 \text{ mA/cm}^2$ . After two weeks RT oxidation the oxidized PS was removed with 24% HF for 30 minutes. It was then subjected to another week of RT oxidation and the oxidized PS removed with 24% HF for 4 hours, demonstrated in Figure 6 to be an efficient means of enlarging the hollow channels. Two HT oxidation stages were then used, first at 800 °C for two hours, centre column, then a further stage at 900 °C for another two hours, right-hand column, to study the effects of both temperature and time.

Under these conditions widely differing core and channel sizes are produced after anodization and RT oxidation. For the highest fluence, Figure 7a, a large, crystalline silicon core is present at the base of the hollow channel. For the intermediate fluence, Figure 7b, the hollow channel has a bright region beneath it, arrowed, comprising low porosity PS. At the lowest fluence, Figure 7c, a hollow channel of about 300 nm width  $\times$  100 nm height is formed with no core or low porosity zone beneath it.

After HT oxidation at 800 °C or 900 °C the overall channel shape and size is unchanged, expected since  $T$  is not high enough to cause significant compaction of the OPS layer at  $j = 150 \text{ mA/cm}^2$ . For the lowest fluence, after HT oxidation the channel remains fully hollow. This is the ideal situation; whereas at higher fluences expansion of the core or low porosity zone at the base of the hollow channel strongly disrupts its shape and size after HT oxidation. At the highest fluence the core size increases, resulting in a smaller channel height. The effect at the intermediate fluence is even more dramatic since the channel changes from being hollow before HT oxidation to the central portion nearly closed off afterwards. This is an important observation as it shows that there is an intermediate range of fluence between that which is low enough to produce no zone of decreased porosity as in Figure 7c and that which is high enough to produce a solid core as in Figure 7a, where a zone of low porosity silicon can partially or even fully close off the OPS channel after HT oxidation. We conclude that using a high fluence which results in a large core is not necessarily detrimental to channel formation, so long as one does not wish to completely oxidize it.

The reason for the different behaviour versus fluence is summarised in figure 8 for high  $j$ . The large difference in  $P$  produced at an intermediate fluence between the high  $P$  host and the low  $P$  core

means that during HT oxidation the host contracts whereas the core expands, bulging into the empty channel. For a fully crystalline core, figure 8a, thermal oxide growth around the core causes it to expand, though at a slower rate than for the low porosity core, so having a less pronounced effect. It is worth noting that we do not observe this same effect whereby an intermediate fluence causes blockage of the OPS channel for anodization at low  $j$ . This is because of a lower difference in porosity between the host and the core, both tending to expand during HT oxidation.

Also shown in Figure 7b is a channel produced under the same fluence, anodization and RT oxidation conditions but with a single HT oxidation stage of 1000 °C. Again the low porosity zone produces a similar bulge into the channel though the resulting channel is smoother as  $T$  is now high enough to allow viscous flow of the OPS. This property is used later in figure 12 to produce smooth, elliptical and circular channels.

#### 4.4. EFFECTS ABOVE THE END-OF-RANGE REGION

We now consider the effect of ion irradiation on the zone above the end-of-range depth where the defect density is much lower, figure 1a. Figure 9a shows the effect of different fluences where the sample was anodized at  $j = 60\text{mA/cm}^2$  ( $P \sim 59\%$ , figure 2c) so that the OPS layer thickness at unirradiated areas is almost unchanged after HT oxidation at 1000 °C. However, a clear reduction in thickness occurs at the irradiated lines, with the effect getting stronger with increasing fluence.

To explain this, Figure 9b shows a schematic of the different zones produced by high energy ion irradiation followed by anodization. For both high and low fluences there is a high porosity zone at the end-of-range and there may also be a core present at high fluences. Even though the defect density along the initial portion of the ion trajectory is relatively low, the porosity here is still increased compared to the surrounding unirradiated host. After RT oxidation all PS has an increased porosity, Figure 9c, and a hollow channel forms where the highest porosity PS at the end-of-range is removed. During HT oxidation, Figure 9d, the higher porosity zone above the hollow channel is more readily fully oxidized than the surrounding host, resulting in its compaction and reducing the hollow channel height.

Now that this has been identified as a factor influencing vertical channel dimensions, a similar argument may be made for a change in the horizontal channel dimensions during HT oxidation. For low/high  $j$  any volume expansion/contraction of the surrounding OPS host may shrink/expand the horizontal channel width. We look for this effect in the following section.

In summary we have identified two mechanisms which reduce the dimensions of the hollow channels, the growth of any crystalline or low porosity core from beneath, which occurs only for high  $j$ , and a compaction of the zone above, which occurs for any  $j$  if the fluence is high. The effect becomes more pronounced with fluence, so that for an optimally low fluence it does not happen.

## 5. CHANNEL FABRICATION IN REGIMES OF DIFFERENT $j$ & $T$

With an improved understanding of the effects of different fluences on channel and core formation we now study and compare examples of channels produced in different regimes of  $j$  &  $T$  to see how OPS layer expansion/compaction at low/high  $j$  and viscous flow at high  $T$  can be used to alter the channel size and shape.

### 5.1. HIGH $j$

We first consider the behaviour observed for anodization at  $j = 150 \text{ mA/cm}^2$  at low and high  $T$ . After irradiation and RT oxidation, figure 10 left column, one batch of samples underwent HT oxidation at 800 °C, centre column, where no layer compaction or viscous flow of the OPS is expected, and another batch at 1000 °C, right column, where full oxidation, layer compaction and viscous flow of the OPS is expected. Channels were produced for three different fluences, decreasing from top to bottom. As expected, the OPS layer thickness is unchanged after HT oxidation at 800 °C with no evidence of viscous flow. Figure 11a shows the channel width and height before and after HT oxidation. After HT oxidation the channel width is unchanged whereas the channel height is slightly reduced. We attribute this to the growth and expansion of the crystalline core (high fluence) and low porosity zone (lower fluence) beneath the channel, rather than overall compaction of the OPS layer. In this regime of high  $j$  and low  $T$ , channel fabrication is straightforward, though without viscous flow it is not possible to produce smooth, symmetrical channel shapes.

The OPS layer thickness is significantly reduced at  $T = 1000 \text{ °C}$ . Due to lateral compaction of the OPS at the exposed, cleaved surface the remaining cores protrude at high fluence, figure 10a. Further vertical compaction of the OPS layer also occurs, shown by the double-headed arrow, owing to the higher porosity of the zone above the cores due to ion induced damage; this spectacular example occurred here because  $j$  is much higher compared to figure 9, so the PS above the channels is already more porous. OPS layer compaction does indeed reduce the channel size, seen in figure 10b, where the additional bulge of the low porosity zone into the channel is shown at higher magnification, further reducing the hollow channel height. For the lowest fluence, figure 10c, the small channels in the anodized PS become fully

closed, the dashed ellipse shows where the channels should be located. We conclude that high  $T$  does help to smoothen the channel profile through viscous flow, and the resultant OPS layer compaction reduces channel height at high  $j$ . However, care is needed to choose a fluence such that the channels are not completely closed off. Figure 11a plots the trend for channel width and height after HT oxidation at both temperatures, where the decrease in channel height and reduced channel width for higher  $T$  is apparent.

## 5.2. LOW $j$

We now consider irradiation and anodization at a low  $j = 30 \text{ mA/cm}^2$  followed by high  $T$  oxidation at  $1000^\circ\text{C}$ . High  $T$  is used here to study the effect of viscous flow on the channel shape in OPS without them being destroyed by layer compaction as for high  $j$ . This study makes use of our above observation that a large core beneath a hollow channel in PS does not necessarily impede its formation in OPS, so long as one does not wish to fully oxidize the core.

Figure 12 shows cross-section SEM images of cores and channels at four different fluences, decreasing from top to bottom. After anodization, left column, at high fluences there is a large, crystalline core beneath a large zone of high porosity PS. For lower fluences there is a low porosity core beneath a smaller zone of high porosity PS. After RT oxidation for 12 days and brief immersion in 2% dilute HF the high porosity PS is removed, central column. After HT oxidation, right column, the host OPS expands since it is of low  $P$ .

As found in figure 10, the real channel profiles after HT oxidation are difficult to observe at high fluences on a cleaved cross-section, so a different approach was used here. We exposed an interior channel cross-section using a focused gallium ion beam (FIB) to selectively cut a cross-section for SEM imaging. Owing to the nature by which the hollow channels are exposed, all other features including the remaining partially-oxidized core beneath it is not observed in cross-section SEM images. Now, viscous flow results in symmetric, elliptical channels produced at high fluences, and smaller circular channels for a lower fluence before the channel disappears at the lowest fluence. Figure 11b plots the channel height and width versus fluence before and after HT oxidation. The channel height remains unchanged owing to the absence of layer compaction, whereas the width is clearly reduced after HT oxidation, with a minimum, nearly circular, channel size of  $70 \text{ nm (width)} \times 60 \text{ nm (height)}$  produced.

For low  $j$ , whether the channel height changes after HT oxidation at high  $T$  depends on opposing processes. The low  $P$  host increases in thickness, tending to enlarge the channel height. As observed in figure 9, for high fluences the zone above the hollow channel may be compacted at high  $T$ . As observed in figure 7, at high fluences a crystalline core beneath the channel will expand and may reduce the hollow

channel area, and a low porosity core is even more damaging in this respect, at least for high  $j$ . We interpret the results in figure 12 as showing that under these conditions, there is little compaction of the zone above the channel since  $j$  is very low, and any growth of the crystalline core at high fluence is countered by the expansion of the OPS layer thickness.

As previously discussed, for low  $j$  we may expect a reduced channel width owing to expansion of the OPS volume. The result of these different factors is an elliptical channel which is highly smooth and regular as the OPS layer has become viscous and forms a surface to minimize surface energy. For lower fluence, the channel area is reduced owing to the more rapid growth of the low porosity core and the smaller hollow channel height, figure 12c, where now a perfectly cylindrical channel is formed. At lower still fluence the channel is fully closed.

We conclude that for low  $j$ , the absence of layer compaction allows a better control over the channel dimensions, allowing widths down to  $\sim 60$  nm to be produced. High  $T$  produces regular, symmetric shapes and helps to smoothen channels.

## 6. CONCLUSIONS

This work is a vital step in developing this process to allow three dimensional integrated micro-and nano-channel arrays for fluidics applications, which we are currently developing. We have conducted a thorough study of the effect of processing parameters such as irradiation fluence, anodization current density, room temperature and high temperature oxidation conditions and developed simple oxidation models to explain the observed trends. We have identified conditions where highly smooth, symmetric channels can be produced with high oxidation temperatures to induce viscous flow and a low anodization current density so that the channels are not destroyed by layer compaction. Under these conditions, and somewhat counter-intuitively, a high ion fluence which results in a large silicon core beneath the channel produces excellent elliptical channels.

## SUPPORTING INFORMATION

**Line Fluence:** The standard unit to quantify the number of ions used for irradiation is the areal fluence,  $\psi_a$ , defined as the number of ions incident upon a given surface area, ions/cm<sup>2</sup>. However, for irradiating narrow regions where the surface line width is smaller than the size of ion lateral straggling effect at the end-of-range, a more useful parameter is the line fluence,  $\psi_l$ , given by the number of ions used for irradiating a line of zero width per centimetre of line length. We use the unit of line fluence for all irradiations in this paper.

**ACKNOWLEDGMENTS**

We wish to thank the International Atomic Energy Agency for partial support under the CRP Project No. F11016. This work was partly performed at SSLS under NUS Core Support C-380-003-003-001, at NUSNNI under NUS Core Support C-380-000-003-001, and National Research Foundation project NRF-CRP8-2011-06.

## Figures

**Figure 1.** Schematic of fabrication of buried horizontal channels. (a) Simulated plot for defect distribution versus depth for 1 MeV protons in silicon. The box size is  $20 \times 20 \mu\text{m}$ . Generated using the SRIM (Stopping and Range of Ions in Matter) code<sup>22</sup>. (b) low fluence irradiation of lines and extended areas, producing high defect concentration at the end of range depth. (c) electrochemical anodization to produce a low porosity PS host with high porosity PS end-of-range regions. (d) current funnelling into the end-of-range region during anodization. (e) RT oxidation and removal of highly porous PS using dilute HF, (f) HT oxidation to convert remaining low porosity PS into OPS.

**Figure 2.** (a) Anodized p-type silicon porosity versus wafer doping density for different  $j$  [data from Ref. 1]. (b) PS layer thickness change upon HT oxidation versus  $j$ . A pre-oxidation step of  $300 \text{ }^\circ\text{C}$  for 30 minutes was used to stabilize the porous texture<sup>14</sup>. (c) Porosity of anodized PS layer versus  $j$ . (d) Measured thickness change of anodized layer versus HT temperature for different  $j$ .

**Figure 3.** Cross sectional view of a silicon core irradiated with  $10^{11}$  ions/cm. (a) before oxidation and (b) after HT oxidation.

**Figure 4.** (a) AFM image of OPS surface for  $j = 300 \text{ mA/cm}^2$  and HT oxidation at  $T = 700 \text{ }^\circ\text{C}$  for 4 hours. (b) plot of r.m.s. roughness versus  $j$  for  $T = 1000 \text{ }^\circ\text{C}$  for 2 hours.

**Figure 5.** Three adjacent channels in PS with a  $1 \mu\text{m}$  period, formed by 100 keV proton irradiation. Anodized at  $j = 300 \text{ mA/cm}^2$ . The line fluences are: (a)  $2 \times 10^9/\text{cm}$ , (b)  $6 \times 10^9/\text{cm}$ , (c)  $1.2 \times 10^{10}/\text{cm}$ , (d)  $1.8 \times 10^{10}/\text{cm}$ , (e)  $4 \times 10^{10}/\text{cm}$ , (f)  $1 \times 10^{11}/\text{cm}$ .

**Figure 6.** Study of the effect of RT oxidation on the removal of oxidized PS around the core for a fluence of  $1 \times 10^{10}/\text{cm}$  of 250 keV protons. Anodized at  $j = 300 \text{ mA/cm}^2$ .

**Figure 7.** High magnification cross-section SEMs of a study of the effect of oxidation on the growth of the core for different fluences of (a)  $2 \times 10^{10}/\text{cm}$  (b)  $1.6 \times 10^{10}/\text{cm}$  and (c)  $1 \times 10^{10}/\text{cm}$  of 250 keV protons. Anodized at  $j = 150 \text{ mA/cm}^2$ .

**Figure 8.** Schematic for the different effects of fluence on core formation beneath the hollow channel for high  $j$ . Fluence decreases from (a) to (c). Left column: after anodization. Right column: after HT oxidation.

**Figure 9.** (a) cross-section SEM of 250 keV proton irradiation with four line fluences, increasing from left to right, with five lines irradiated at each fluence. The sample was anodized at  $j = 60 \text{ mA/cm}^2$ . Shown

after two RT oxidation and then HT oxidation at 1000 °C. (b) to (d) show a schematic of the irradiation process followed by (b) anodization, (c) RT oxidation, (d) HT oxidation.

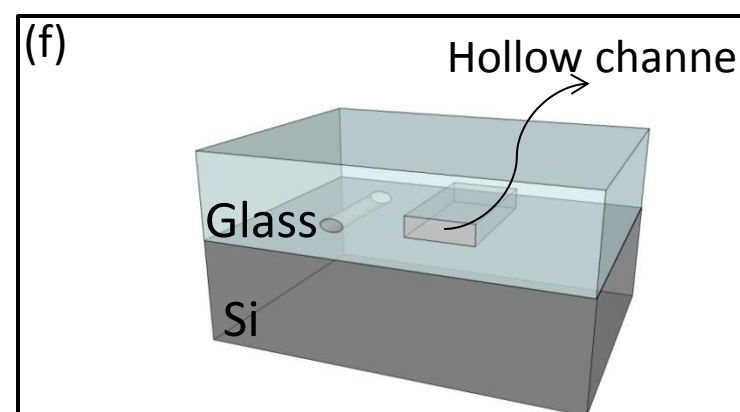
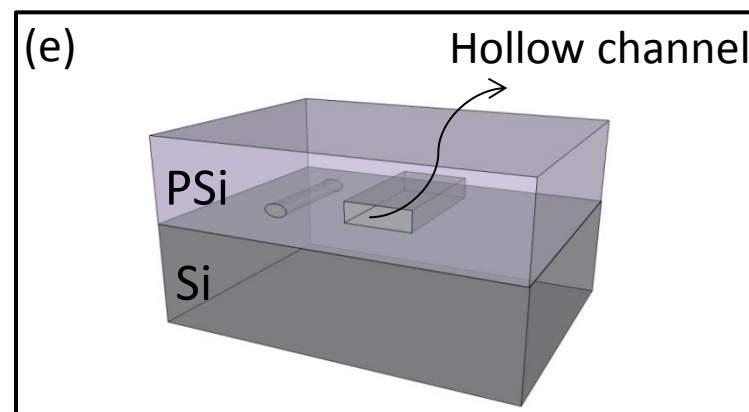
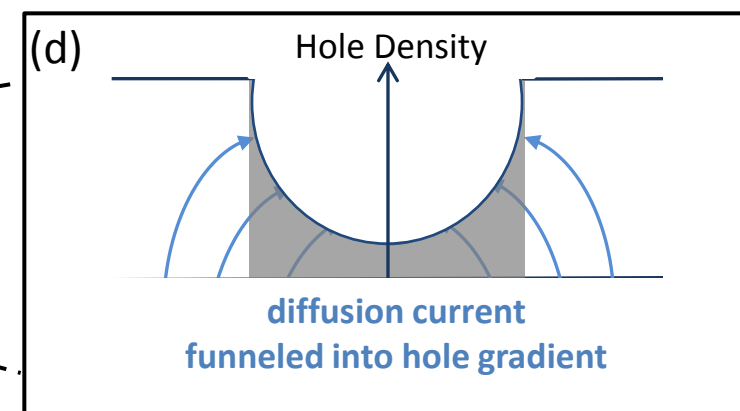
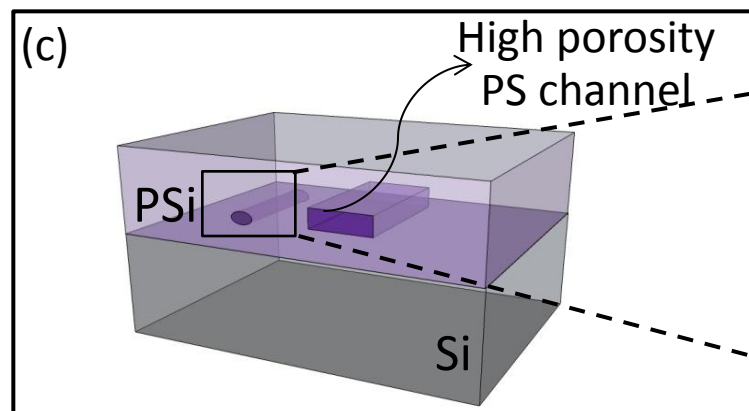
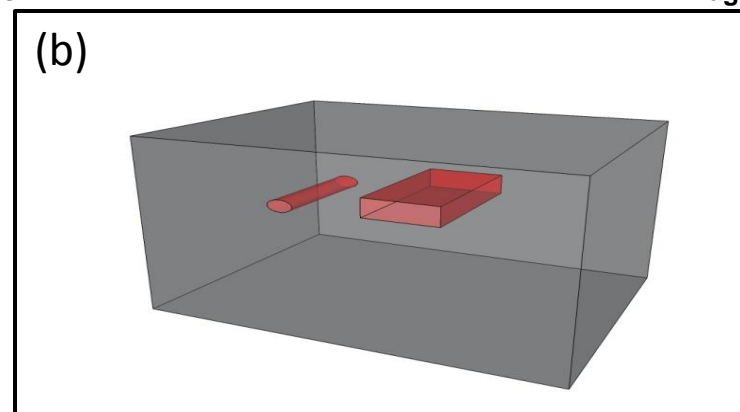
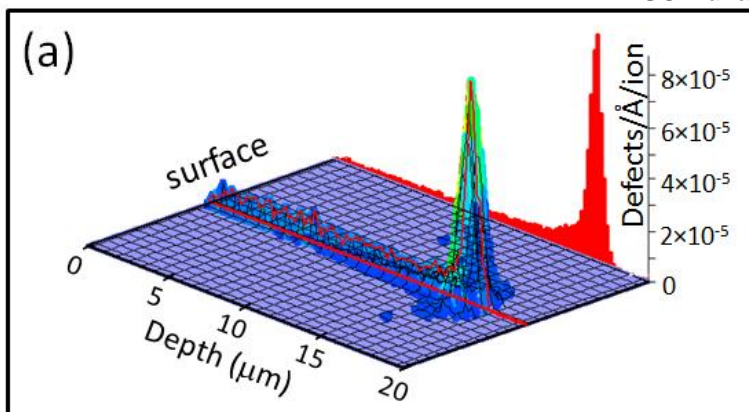
**Figure 10.** 250 keV proton irradiation. Anodized at  $j = 150\text{mA}/\text{cm}^2$ . After PS removal (after 2 weeks oxidation in air and immersion in 24%HF for 5 hours) identical samples underwent HT oxidation at 800°C (centre) and at 1000°C (right side). The line fluences are: (a)  $2 \times 10^{10}/\text{cm}$  (b)  $1.6 \times 10^{10}/\text{cm}$  (c)  $1 \times 10^{10}/\text{cm}$ .

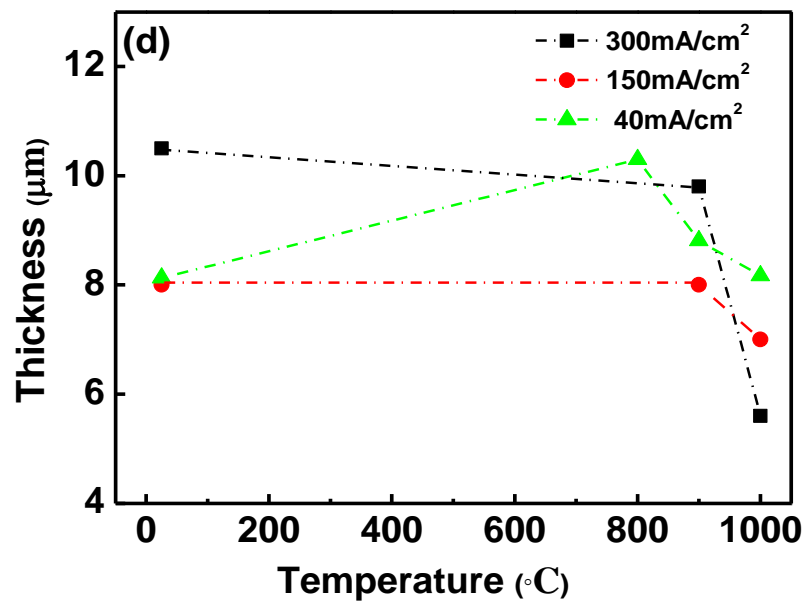
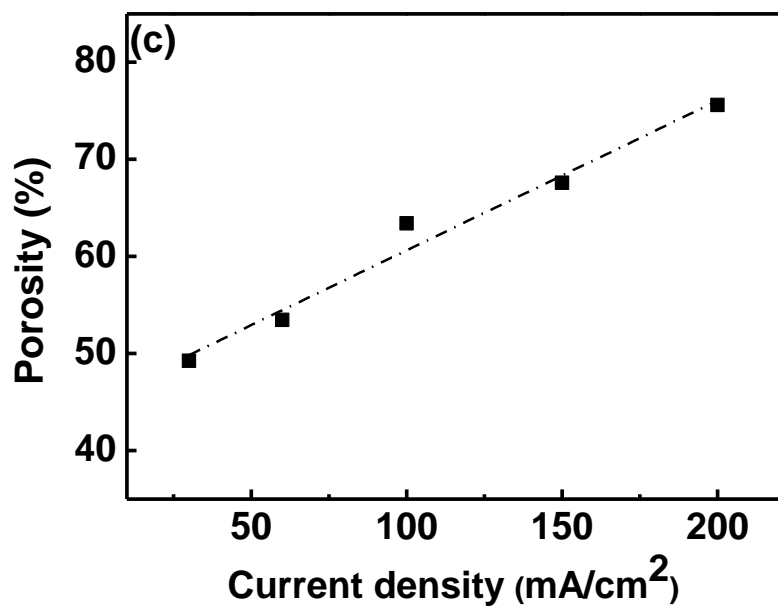
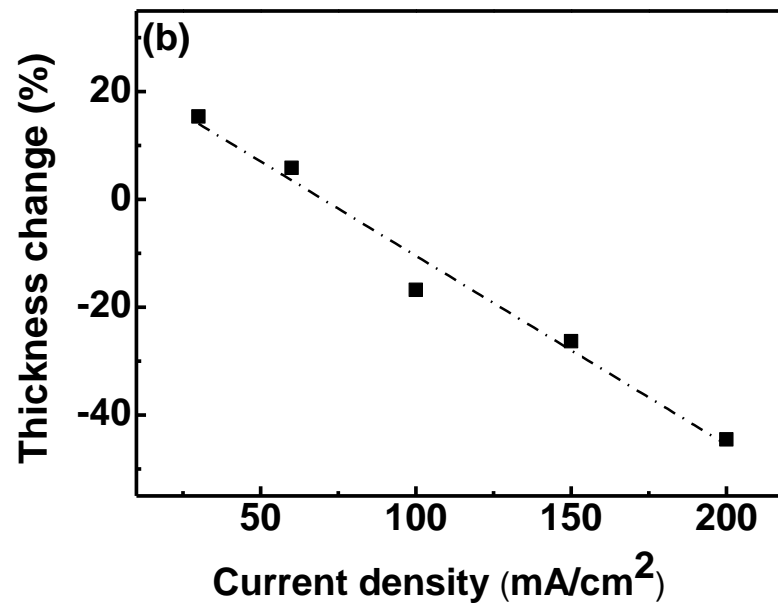
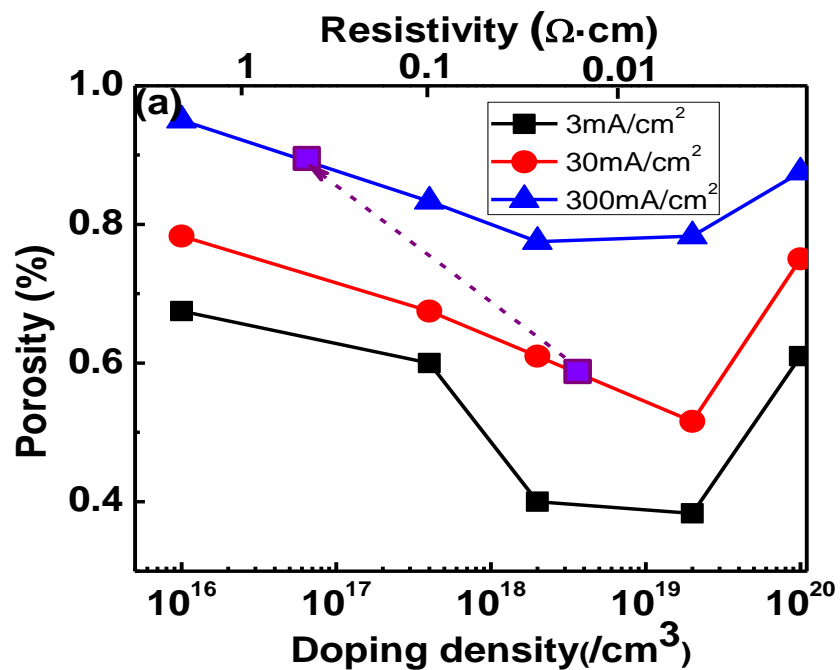
**Figure 11.** Plot of channel dimensions before and after HT oxidation at (a) high  $j$  from figure 10 and (b) low  $j$  from figure 12.

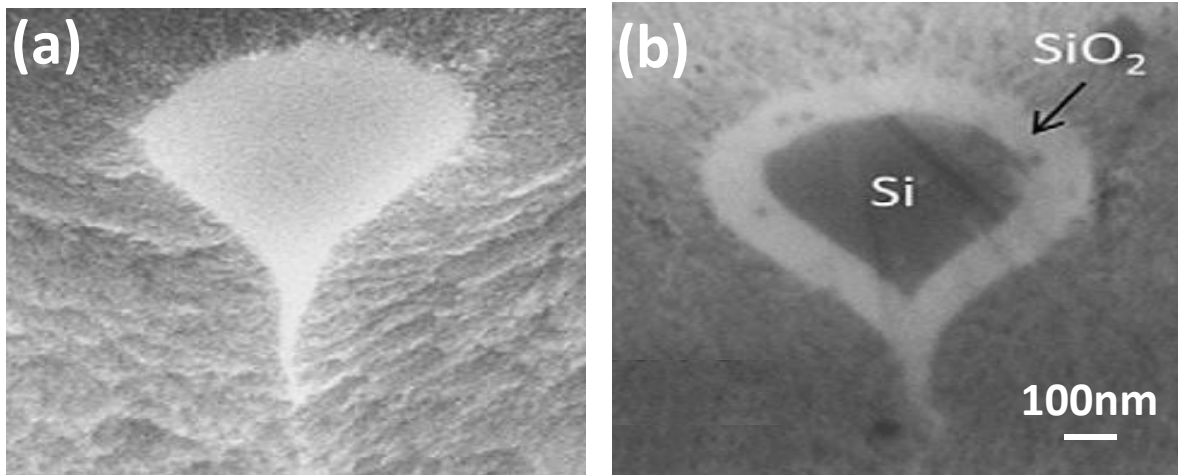
**Figure 12.** High magnification cross-section SEM images of 100 keV proton irradiation with line fluences of (a)  $2 \times 10^{10}/\text{cm}$  (b)  $1.2 \times 10^{10}/\text{cm}$  (c)  $6 \times 10^9/\text{cm}$  (d)  $4 \times 10^9/\text{cm}$ . Anodized at  $j = 30\text{ mA}/\text{cm}^2$  for 3 minutes. OPS removed by RT oxidation for 12 days in air, followed by HT oxidation at  $T = 1000^\circ\text{C}$  (right side).

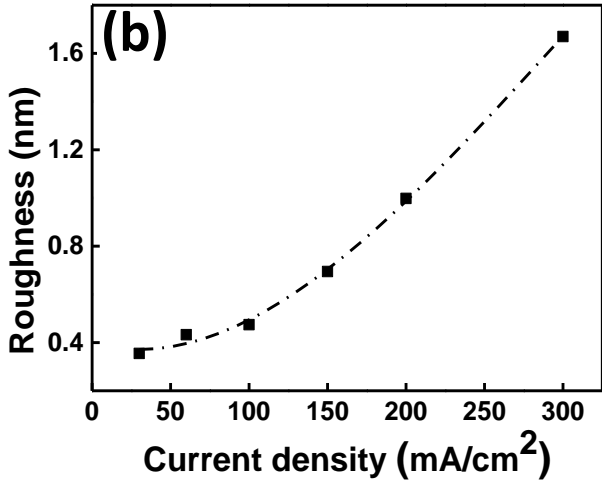
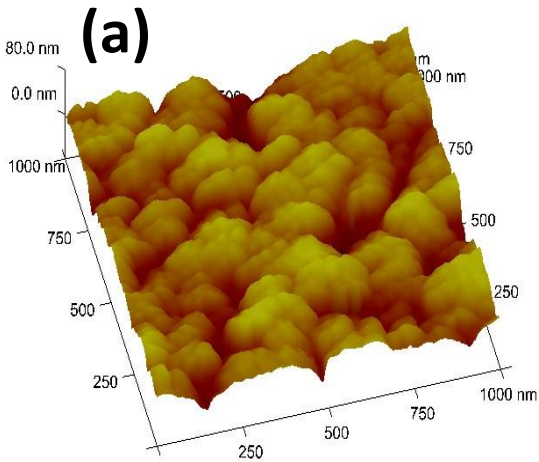
## References

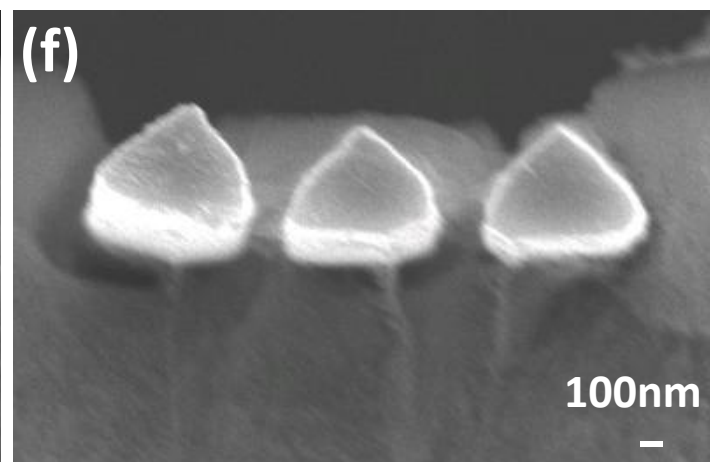
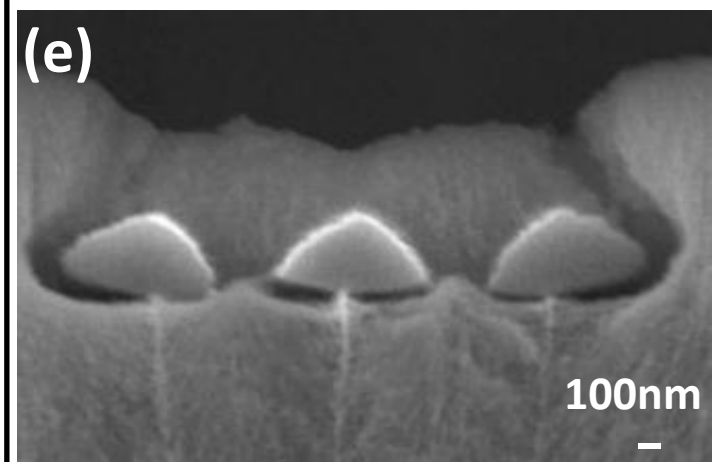
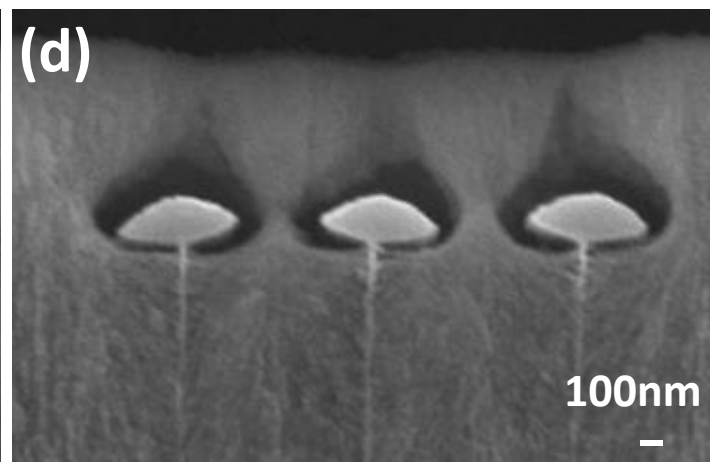
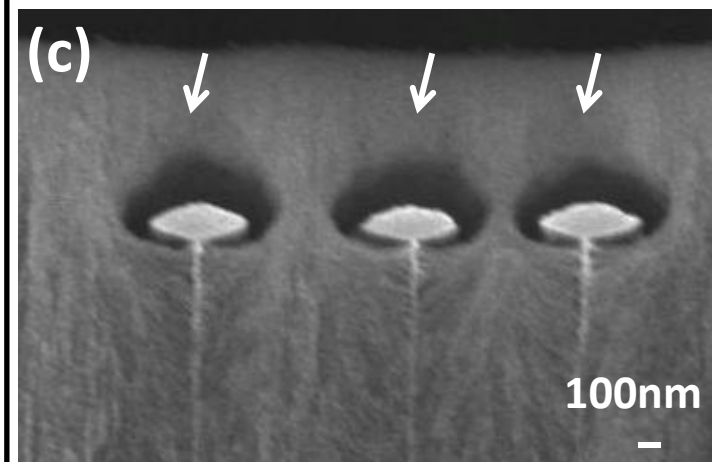
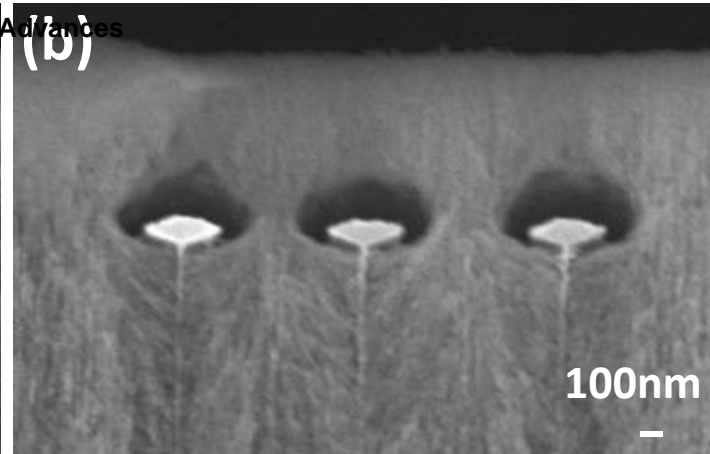
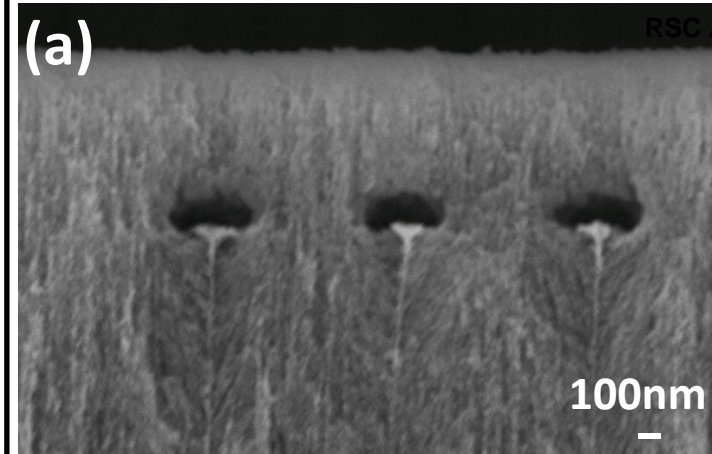
1. S. Azimi, Z. Dang, C. Zhang, J. Song, M. B. H. Breese, C. H. Sow, J. A. van Kan and J. R. C. van der Maarel, *Lab on a Chip*, 2014, **14**, 2081-2089.
2. M. B. H. Breese, D. N. Jamieson and P. J. C. King, *Materials Analysis Using a Nuclear Microprobe*, Wiley, 1996.
3. Z. Y. Dang, J. Song, S. Azimi, M. B. H. Breese, J. Forneris and E. Vittone, *Nuclear Instruments and Methods in Physics Research Section B: Beam Interactions with Materials and Atoms*, 2013, **296**, 32-40.
4. J. Song, Z. Y. Dang, S. Azimi, M. B. H. Breese, J. Forneris and E. Vittone, *ECS Journal of Solid State Science and Technology*, 2012, **1**, P66-P69.
5. E. J. Teo, A. A. Bettioli, M. B. Breese, P. Yang, G. Z. Mashanovich, W. R. Headley, G. T. Reed and D. J. Blackwood, *Opt. Express*, 2008, **16**, 573-578.
6. V. Lehmann, in *Electrochemistry of Silicon*, Wiley-VCH Verlag GmbH, 2002, pp. 97-126.
7. S. Azimi, Z. Y. Dang, J. Song, M. B. H. Breese, E. Vittone and J. Forneris, *Applied Physics Letters*, 2013, **102**, 042102.
8. M. Napoli, J. C. T. Eijkel and S. Pennathur, *Lab on a Chip*, 2010, **10**, 957-985.
9. M. Elwenspoek, T. S. J. Lammerink, R. Miyake and J. H. J. Fluitman, *Journal of Micromechanics and Microengineering*, 1994, **4**, 227-245.
10. Y.-J. Oh, T. C. Gamble, D. Leonhardt, C.-H. Chung, S. R. J. Brueck, C. F. Ivory, G. P. Lopez, D. N. Petsev and S. M. Han, *Lab on a Chip*, 2008, **8**, 251-258.
11. A. T. Woolley and R. A. Mathies, *Proceedings of the National Academy of Sciences*, 1994, **91**, 11348-11352.
12. J. T. Mannion, C. H. Reccius, J. D. Cross and H. G. Craighead, *Biophysical Journal*, **90**, 4538-4545.
13. K. Imai, *Solid-State Electronics*, 1981, **24**, 159-164.
14. J. J. Yon, K. Barla, R. Herino and G. Bomchil, *Journal of Applied Physics*, 1987, **62**, 1042-1048.
15. G. Ahmed, R. Boudjemaa, H. Aomar, B. Daniel and S. Abdelkader, *Semiconductor Science and Technology*, 2012, **27**, 105017.
16. A. E. Pap, K. Kordás, G. Tóth, J. Levoska, A. Uusimäki, J. Vähäkangas, S. Leppävuori and T. F. George, *Applied Physics Letters*, 2005, **86**, 041501.
17. Y. H. Ogata, T. Tsuboi, T. Sakka and S. Naito, *Journal of Porous Materials*, 2000, **7**, 63-66.
18. J. Salonen, V. P. Lehto and E. Laine, *Applied Surface Science*, 1997, **120**, 191-198.
19. R. B. Marcus and T. T. Sheng, *Journal of The Electrochemical Society*, 1982, **129**, 1278-1282.
20. B. E. Deal and A. S. Grove, *Journal of Applied Physics*, 1965, **36**, 3770-3778.
21. E. A. Irene, E. Tierney and J. Angilello, *Journal of The Electrochemical Society*, 1982, **129**, 2594-2597.
22. J. F. Ziegler, M. D. Ziegler and J. P. Biersack, *Nuclear Instruments and Methods in Physics Research Section B: Beam Interactions with Materials and Atoms*, 2010, **268**, 1818-1823.





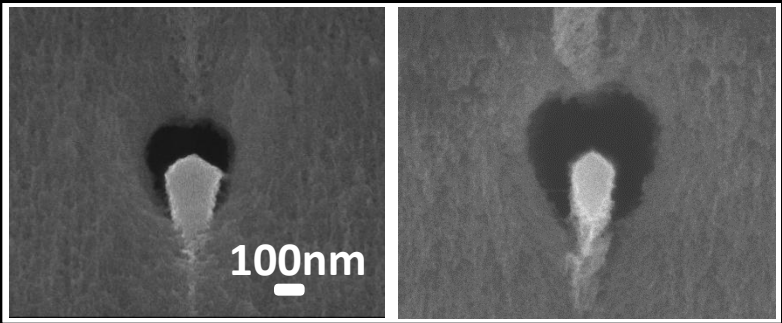


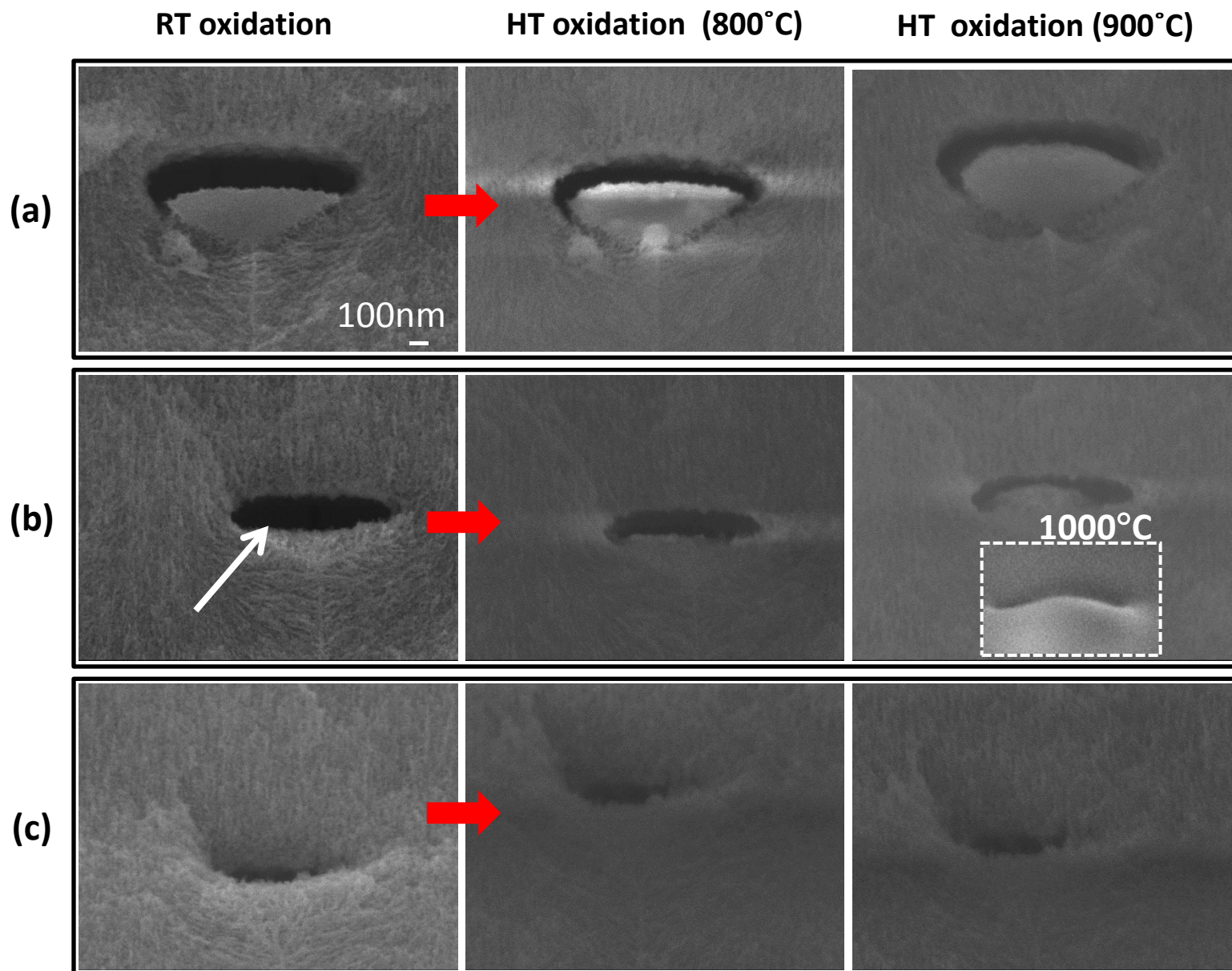


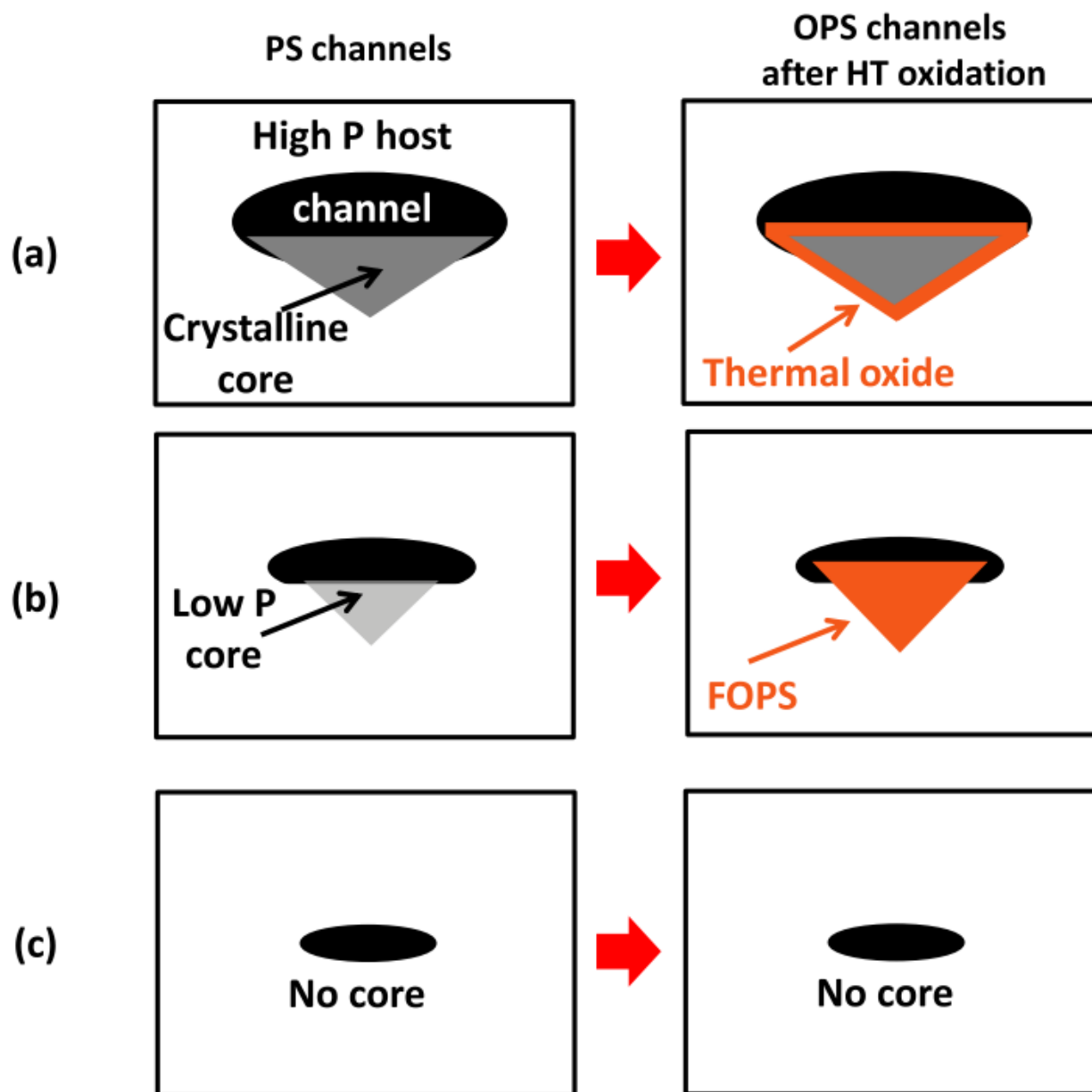


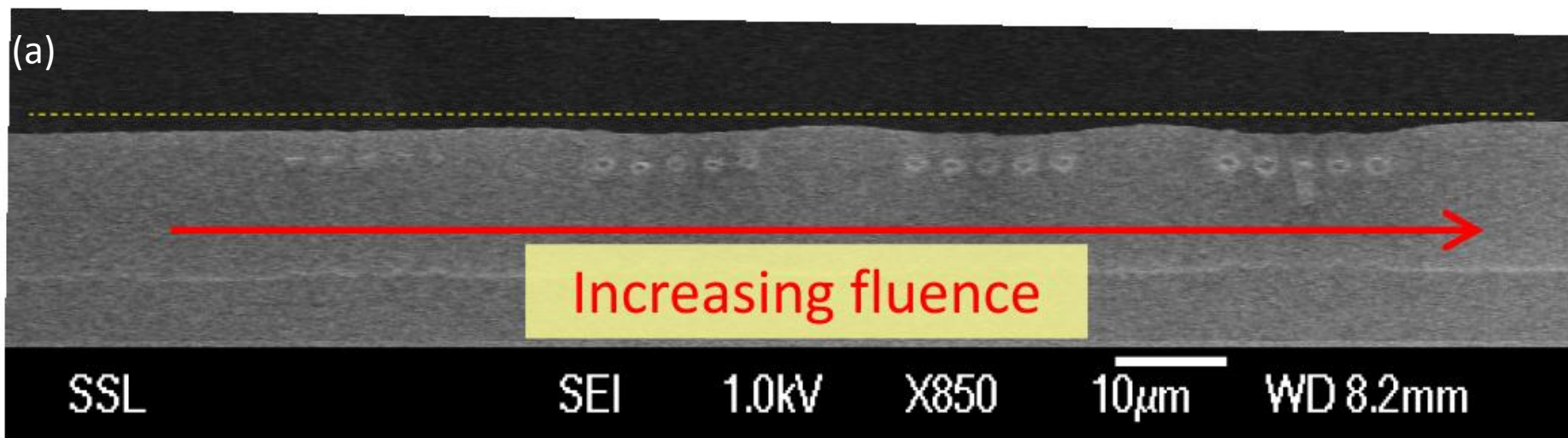
1st RT oxidation

2<sup>nd</sup> RT oxidation









(b) Irradiated region

(c) P increased at all PS regions

(d)

After Anodization

After RT oxidation

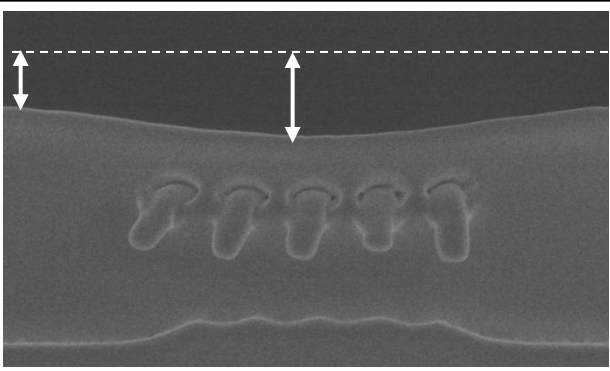
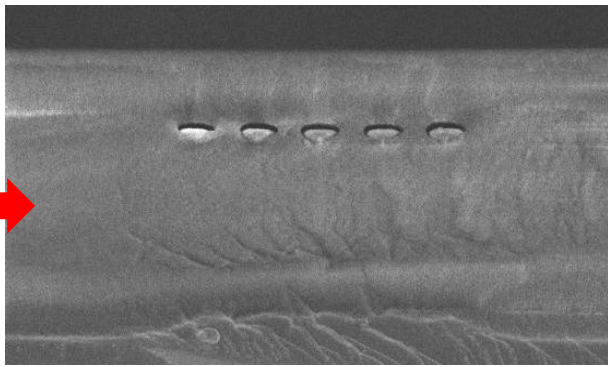
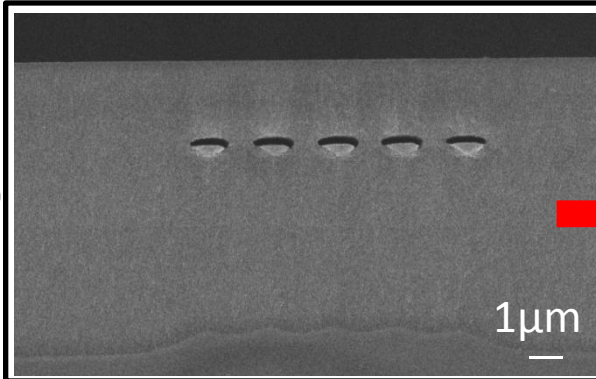
After HT oxidation

RT oxidation

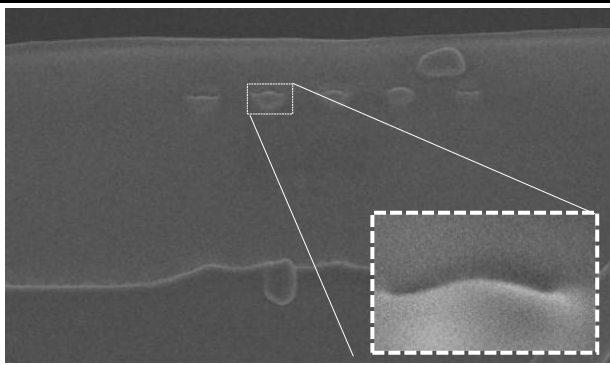
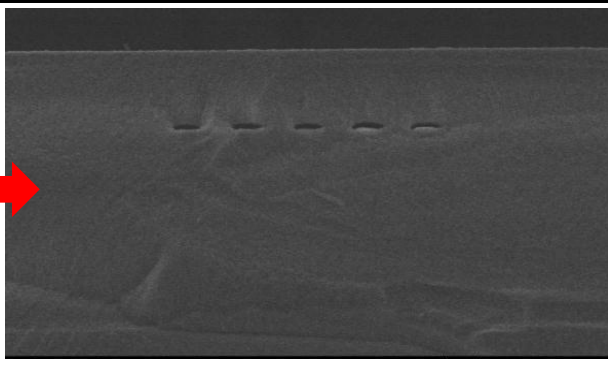
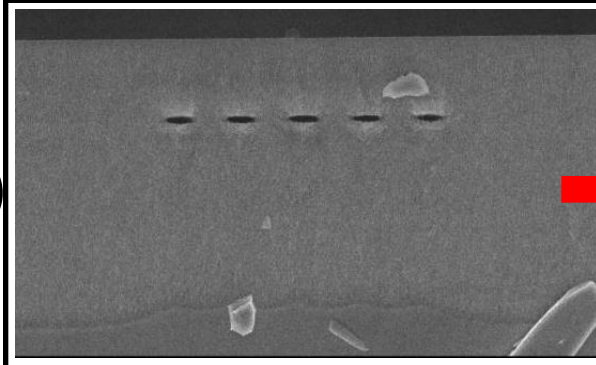
HT oxidation ( 800°C)

HT oxidation (1000°C)

(a)



(b)



(c)

